Wu et al. *Microsystems & Nanoengineering* (2025)11:108
https://doi.org/10.1038/s41378-025-00927-1

Microsystems & Nanoengineering
www.nature.com/micronano

ARTICLE Open Access

# Tetrahedral-modified magnetic nanorobotic probe for enhanced imaging of cancer-related miRNA

Xue Wu[1], Huijie Bai[1], Lingfeng Jiang[1], Cuiping Mao[1], Yi Li[1], Diangeng Li[2]✉, Yong Wang[1,3]✉, Shan Liu[4]✉ and Jinhong Guo[1,3,5]✉

**Abstract**

Sensitive and rapid imaging of intracellular cancer-related miRNA holds great potential for early diagnosis and treatment monitoring of cancer. However, most imaging probes are constructed on nanoparticles that rely on passive diffusion to interact and bind with the target substance, resulting a long response time and a low target recognition capability due to the solution viscous resistance. Herein, we reported a DNA tetrahedral-modified magnetic nanorobotic probe (MNP) that performed framework nucleic acid-located catalytic hairpin assembly (CHA) reaction on the surface of magnetically driven nanorobot. The tetrahedral structure not only endowed the MNP with extremely high structural stability and perfect cell-uptake performance, but its spatial confinement effect made the signal amplification of the hairpin cascade more rapid and efficient. Additionally, the active movement of MNPs enhanced the micro-mixing of fluids and accelerated target capture, significantly reducing reaction time and improving reaction kinetics. This strategy exhibited the enhanced fluorescence signal and can accurately distinguish between miR-21 and various other miRNA sequences. Moreover, the feasibility and versatility of MNPs were also successfully verified in normal and various cancer cells imaging. Therefore, the proposed MNPs are promising candidates for the detection of intracellular biomarkers and extend the design space of self-propelled micro/nanorobots in the field of cancer diagnosis and therapy.

## Introduction

Cancer is one of the leading causes of human death worldwide[1]. The sensitive detection of intracellular cancer-related biomarkers plays an important role in the precision diagnosis, therapeutic management and process monitoring of cancer[2–4]. MicroRNAs (miRNAs) are a type of small, single-stranded noncoding ribonucleic acid molecule with lengths of 19–23 nucleotides, which bind to specific mRNA targets and regulate gene expression after transcription[5]. This regulatory mechanism enables miRNAs to exert vital roles in various cellular activities. And aberrant expression of miRNAs is closely related to the occurrence, development, and metastasis of various cancers[6–8]. MiR-21, as the most commonly upregulated miRNA in almost all types of cancer, is an ideal candidate for broad-spectrum cancer screening[9–11]. The miR-21 detection has been widely used to study the early diagnosis and staging of tumors[12–15]. Therefore, developing an efficient and reliable miR-21 assay is of great importance for the early diagnosis of cancer. Currently, various miRNA detection strategies, including reverse transcription-polymerase chain reaction (RT-PCR), microarray hybridization, and electrochemical sensing, have been widely developed for cancer diagnosis[16–18]. However, these methods usually require destroying cells for nucleic acid extraction, struggle to provide real-time miRNA detection, and lack information on the spatial and temporal distribution of miRNAs. Therefore, there is still a growing demand to develop feasible approaches for

Correspondence: Diangeng Li (lidiangeng@126.com) or Yong Wang (wangyong@cqmu.edu.cn) or Shan Liu (shanliusyy@uestc.edu.cn) or Jinhong Guo (guojinhong@sjtu.edu.cn)
[1]Key Laboratory of Clinical Laboratory Diagnostics (Ministry of Education), College of Laboratory Medicine, Chongqing Medical University, 400016 Chongqing, China
[2]Department of Academic Research, Beijing Ditan Hospital, Capital Medical University, National Center for Infectious Diseases (Beijing), 100015 Beijing, China
Full list of author information is available at the end of the article
These authors contributed equally: Xue Wu, Huijie Bai, Lingfeng Jiang

monitoring miRNAs in living cells to achieve the precise identification of cancers.

In recent years, with the deepening of DNA nanotechnology research, DNA nanoprobes based on framework nucleic acids have been widely used for intracellular biomarkers detection of cancer due to their easy synthesis, highly programmability, controllable size and excellent biocompatibility[15,19,20]. For example, Chen et al. designed three-dimensional tweezers to image and regulate miRNAs in living cells[21]. Lin et al. fabricated a tetrahedral framework DNA-enhanced hybridization chain reaction (HCR) system for detecting membrane and intracellular cancer-related targets[22]. Chen et al. also constructed a cubic DNA nanocage for ratiometric fluorescence detection and imaging of miRNA[23]. Benefiting from the spatial confinement and compact spatial structure of the framework nucleic acids, this strategy was proved to exhibit attractive sensitivity, fast reaction rates as well as favorable stability[24,25]. Notably, although framework nucleic acids can enter the cell via endocytosis with the help of the collision of their own vertices with the cell membrane without transfection reagents, the negative surface charge of oligonucleotides jeopardizes their affinity for the cell membrane[26,27]. More importantly, in the complex fluidic space, the nanoprobes contact with the target mainly by passive diffusion, which is obviously bound by external viscous resistance, resulting in low capturing efficiency and unsatisfactory detection performance. These negative effects are expected to be mitigated if these probes were attached to continuously moving micro/nanocarriers.

Micro/nanorobots are a novel type of active carriers that can effectively convert the chemical fuel (hydrogen peroxide, glucose, and urea) or external energy (ultrasound, magnetism and light) in the surrounding environment into their mechanical propulsion to achieve autonomous movement[28–30]. In contrast to conventional nanoprobes, the self-propelled micro/nanorobots are able to break the constraints of their own irregular Brownian motion and low Reynolds number at the micro and nanoscale, and move controllably in liquid environments with autonomous navigation[31–33]. Simultaneously, micro/nanorobots can be engineered into specified shapes to facilitate their own crossing of biological barriers, surging and delivering cargo to the interest areas[34,35]. They can also form clusters or discrete units guided by external fields to further facilitate mass transfer and collisions with target analytes[36,37]. Given their favorable motion characteristics and easy surface functionalization, micro/nanorobots have been integrated with multiple sensing technologies for rapid detection of biomarkers. As an example, Ju et al. described a class of enzyme-powered micro/nanorobots for DNA sensing[38,39]. They utilized DNA strand displacement to reduce the amount of enzyme assembled on the microrobot thereby slowing down the self-propulsion rate. The proposed microrobot used motion speed as the signal input and can make a sensitive response to the target DNA, which was an exceptional tool for the rapid and simple detection of biomolecules. Due to the cytotoxicity and the depletion of chemical fuels, the advantages of high controllability, long life cycle, and excellent biocompatibility of external field actuation provides a wider range of applications for artificial micro/nanorobots[40]. Based on this, Wang et al. designed an ultrasound-driven micro/nanorobot for single cell real-time miRNA sensing[41]. Under the action of the ultrasound field, the nanorobot could not only quickly entered cells, but also increased the possibility of contact with the target miRNA, completing the efficient and rapid monitoring of intracellular miRNA. In addition, Ma et al. developed a magnetic immunoprobe for enzyme-linked immunosorbent assay[42]. Antibody-modified magnetic nanorobots could be navigated to the target site under a gradient magnetic field and effectively stirred the liquid under a rotating magnetic field, significantly shortening the incubation time and improving the detection efficiency.

In this work, we constructed the self-propelled $Fe_3O_4$@$SiO_2$-DTH magnetic nanorobotic probes (MNPs) by integrating $Fe_3O_4$@$SiO_2$ nanorobots and DNA tetrahedral-based catalytic hairpin assembly (CHA) probes for rapid and sensitive intracellular miRNA imaging (Fig. 1). $Fe_3O_4$ nanoparticles were introduced to act as the inner core for the magnetic field driving. The silica layer was used not only to facilitate the functionalization of carboxyl group and further conjugate to the aminated DTH probes, but also to serve as the protective layer to ensure the integrity of the $Fe_3O_4$ magnetic core in liquid environments. The DTH probes were further modified on the surface of the core-shell structure to form nanorobot-based nucleic acid detection probes. Specifically, the DTH probes consisted of a DNA tetrahedral framework and two hairpin structures (H1 and H2). Hairpin H1 was dual-modified with a Cy5 fluorophore at its 5′ end and a BHQ2 quenching group at a complementary location near to the Cy5 labeled base (Fig. S1a). In the absence of the target, the stem-loop structure of H1 remained closed, bringing Cy5 and BHQ2 into close proximity. This enabled fluorescence resonance energy transfer (FRET), effectively quenching the Cy5 signal. In the presence of miR-21, miR-21 hybridized to the toehold of H1, initiating a strand displacement reaction (SDR) that unfolded the hairpin (Fig. S1b). This unfolding disrupted the Cy5-BHQ2 FRET pair, separating the fluorophore and quencher, thereby restoring Cy5 fluorescence signal. The opened H1 exposed a new site to bind the toehold domain of H2, which subsequently triggered the unfolding of H2 by a second SDR and then squeezed out miR-21. The released miR-21 remained intact and can repeatedly initiate the

opening of another H1 hairpin in the next round of catalytic hybridization assembly (CHA) cycle, significantly amplifying the fluorescence signal. This cascade ensured high sensitivity by generating a strong Cy5 signal. Moreover, the spatial confinement effect of the tetrahedron significantly increased the local concentration of H1 and H2, further enhancing the reaction kinetics. In addition, driven by the external magnetic field, MNPs were precisely navigated to individual cells, promoting their rapid endocytosis. Following this, MNPs accelerated their contact with the target miR-21 through active rotational motion. Besides, the MNPs were not susceptible to intrinsic interference such as nuclease degradation, and showed good biocompatibility, providing rapid, specific and stable signal output for intracellular miRNA imaging.

## Materials and methods

### Materials

$FeCl_3{\cdot}6H_2O$, NaAc, 1-(3-dimethylaminopropyl)-3-ethylcarbodiimide hydrochloride (EDC), 10× TE buffer (100 mM tris(hydroxymethyl) aminomethane (Tris), 10 mM ethylenediaminetetraacetic acid (EDTA), pH 7.4) were received from Aladdin BioChem Technology (Shanghai, China). Ethylene glyco (EG), isopropanol, $NH_3{\cdot}H_2O$, N, N-dimethylformamide (DMF), succinic anhydride (SAA), triethylamine (TEA) and N-hydroxysuccinimide (NHS) were obtained from Macklin (Shanghai, China). Tetraethyl orthosilicate (TEOS), 6-diamidino-2-phenylindole (DAPI) were acquired from Sigma (St. Louis, MO, USA). All oligonucleotides (Table S1) with high performance liquid chromatography (HPLC) purification, were synthesized by Sangon Biotech (Shanghai, China). $Na_3Cit{\cdot}2H_2O$, 3-aminopropyltriethoxysilane (APTES), Tris, $MgCl_2{\cdot}6H_2O$, $Na_2EDTA{\cdot}2H_2O$, boric acid, ammonium persulphate (APS), 30% acryl/bis solution, tetramethylethylenediamin (TEMED), agarose, 4SGelRed dye and TRIzol reagent were purchased from Sangon Biotech. 20 bp DNA marker and 6x loading were supplied by Takara Biotech (Dalian, China). HEK293, Hela, A375, MDA-MB-231 and MCF-7 cell lines were obtained from American Type Culture Collection (Manassas, USA). Dulbecco's Modified Eagle's Medium (DMEM), fetal bovine serum (FBS), and penicillin/streptomycin were

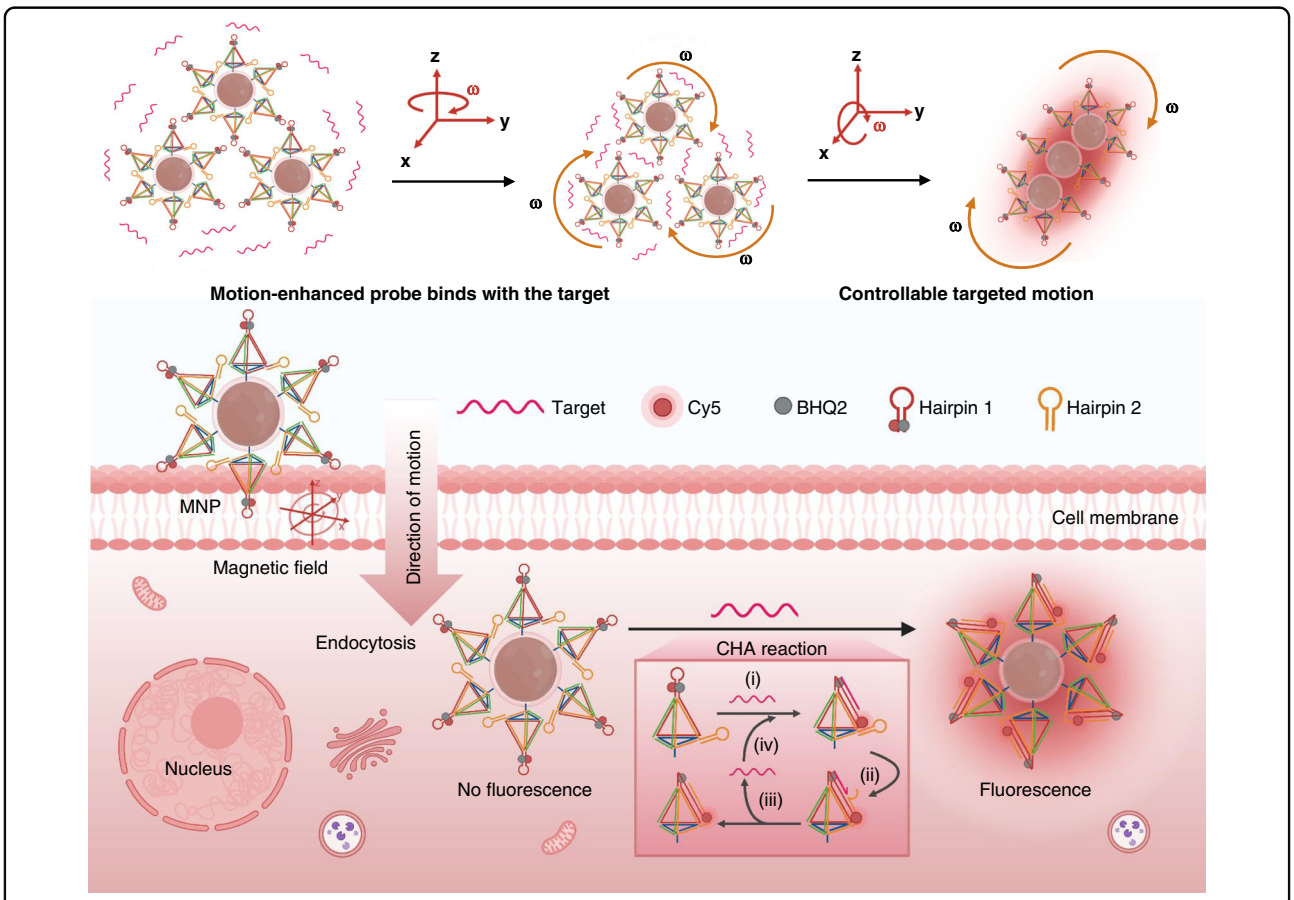


**Fig. 1 Schematic illustration of the mechanism of MNPs for miR-21 imaging in living cells.** The sequence of catalytic hybridization assembly (CHA) reaction: (i) miR-21 binding to H1, (ii) H1 unfolding H2 (iii) miR-21 release, (iv) miR-21 recycling for the next round of CHA

purchased from GIBCO (New York, USA). Cell counting kit-8 (CCK-8) reagent was purchased from MedChemExpress (Monmouth Junction, USA). cDNA reverse transcription kit and the SYBR qPCR Master Mix Kit were purchased from Vazyme (Nanjing, China). All other chemical reagents used were of analytical grade and were provided by Chuandong Chemical Group (Chongqing, China).

Scanning electron microscopy (SEM) and energy dispersive spectrometer (EDS) images were taken on a SU8020 microscope (Hitachi, Japan) at 3.0 kV. Transmission electron microscopy (TEM) images were obtained on a Tecnai G2 12 microscope (FEI, USA) at 120 kV. The saturation magnetization curves were measured by SQUID-VSM magnetometer (Quantum Design, USA). Gel electrophoresis analysis was carried on an EPS300 electrophoresis system (Tanon, China), and imaged on a Tanon mini space1000 (Tanon, China). Atomic force microscope (AFM) images were recorded on a Dimension Icon (Bruker, Germany). Fluorescence spectra were detected on a FL970 fluorescence spectrophotometer (Techcomp, China). Dynamic light scattering (DLS) and zeta potential measurements were performed on a NS-90Z Plus instrument (OMEC, China). Flow cytometry (FCM) analysis was performed using a SA3800 flow cytometer (Sony, Japan). The viscosity of solutions was measured at 60 rpm, using a viscometer (LICHEN, China). The cell cytotoxicity was evaluated by using an Infinite 200 PRO microplate reader (Tecan, Switzerland). Confocal fluorescence images were acquired by LSM980 confocal laser-scanning microscope (CLSM) (Zeiss, Germany). qRT-PCR was carried on a QuantStudio 1 Plus real-time PCR machine (Applied Biosystems, USA).

## Methods

### Preparation of DNA tetrahedron probes

The DTH probe consists of a tetrahedral framework (S1–S4) and two hairpins (H1 and H2). First, four single-stranded DNA (ssDNA) (S1–S4) were mixed in equal molar in TM buffer (Tris 10 mM, $MgCl_2{\cdot}6H_2O$ 50 mM, pH 8.0). Two kinds of hairpins were also diluted in TM buffer, respectively. Next, the mixture (S1–S4) and hairpin solutions were heated to 95 °C for 5 min and naturally cooled down to room temperature, respectively. Next, the equal amounts of DTH (S1–S4), H1 and H2 were mixed and incubated in 37 °C for 60 min to prepare DTH probes via sticky-end hybridization. The DTH probe solution was stored under 4 °C in the dark for no more than one week.

### Synthesis of carboxyl-functionalized $Fe_3O_4@SiO_2$ nanoparticles

$Fe_3O_4$ nanoparticles were synthesized through a hydrothermal method in accordance with previous report with slight modifications[43]. First, $FeCl_3{\cdot}6H_2O$ (1.054 g) and $Na_3Cit{\cdot}2H_2O$ (0.20 g) were added to EG (10 mL) and stirred magnetically for 30 min. Second, NaAc (1.20 g) was dissolved in EG (10 mL) by ultrasound for 10 min. Then, the above two EG solutions were mixed under magnetic stirring and stirred for another 10 min to obtain a uniform solution. Subsequently, the mixture was sealed in a Teflon-lined stainless-steel autoclave (100 mL capacity) and heated at 200 °C for 12 h. After cooling down to room temperature, the reaction product $Fe_3O_4$ was collected by an external magnetic field and washed 3 times with deionized (DI) water and ethyl alcohol (EtOH), respectively. The collected $Fe_3O_4$ was resuspended in EtOH for further use.

The sol-gel method was adopted to coat $SiO_2$ in the surface of $Fe_3O_4$[44]. $Fe_3O_4$ (4 mg) was dispersed into a mixture of DI water (5 mL) and isopropanol (25 mL), and the mixture was sonicated for 15 min. Then, $NH_3{\cdot}H_2O$ (0.5 mL) was added into the obtained dispersion and mechanically stirred for 10 min. Next, TEOS (40 μL) was added slowly and the mixture was stirred at room temperature for 4 h. After that, $Fe_3O_4@SiO_2$ was obtained by magnetic separation and washed several times with DI water and EtOH.

In the process of functionalization, $Fe_3O_4@SiO_2$ (4 mg) was first dispersed in EG (20 mL) and APTES (200 μL) was then added into the solution and stirred for 24 h. The resulting product $Fe_3O_4@SiO_2$-$NH_2$ was collected by magnetic separation and then washed with EtOH several times. After the $Fe_3O_4@SiO_2$-$NH_2$ was re-dispersed in DMF (10 mL), SAA (50 mg) and TEA (52.1 μL) were added to the mixture and stirred for another 24 h at room temperature. Finally, the obtained $Fe_3O_4@SiO_2$-COOH was dispersed in EtOH for further use.

### Fabrication of MNPs

MNPs were prepared by covalently coupling aminated DTH probes with carboxylated $Fe_3O_4@SiO_2$ nanoparticles. To activate the carboxyl-modified $Fe_3O_4@SiO_2$, $Fe_3O_4@SiO_2$ (50 μg) was reacted with EDC (5 mg) and NHS (2.5 mg) in 100 μL TM buffer for 30 min. Then, DTH probes (1 μM, 50 μL) were combined with the activated $Fe_3O_4@SiO_2$-COOH at room temperature for 6 h. After that, surplus DTH probes were removed by magnetic separation and MNPs were resuspended in TM buffer for further use.

### Electrophoresis and fluorescence characterization of DTH probes

To verify the CHA capability and characterize the self-assembly of DTH probe, the samples were prepared by the stepwise addition of DNA strands (1 μM) in TM buffer. CHA reaction was analyzed by 8% native polyacrylamide gel electrophoresis (PAGE) at a voltage of 110 V for 40 min. 3% agarose gel electrophoresis was

performed for DTH probe characterization and a voltage of 100 V was applied for 60 min. For assessing the stability, DTH probes (1 μM) were incubated in DMEM with 10% FBS solution from 0 to 8 h, respectively. Finally, each sample was determined by 3% agarose gel electrophoresis.

To evaluate the reaction kinetics, DTH probes (250 nM) were incubated with miR-21 (100 nM) for 2.5 h and the real-time fluorescence was recorded every second by fluorescence spectrophotometer. In addition, to investigate the fluorescence signal stability of DTH probe in 10% FBS, the fluorescence intensity of Cy5 at 666 nm was detected at an excitation wavelength of 649 nm.

### Design of the magnetic manipulation platform

The home-made magnetic field generator included a CCD camera, a microscope, a function generator, a power amplifier, and the magnetic field generator. The magnetic field generator used in the experiment is a Helmholtz coil composed of three pairs of parallel coils. When a current flows through an electromagnetic coil, a uniform magnetic field is generated within the coil. Various function signals from the function generator were amplified to drive the magnetic field generator to produce the required magnetic field. The magnetic field's strength and direction could be adjusted in real time by changing the current supplied to the electromagnetic coils. The magnetic control system was used in conjunction with a microscope for observing and tracking MNPs. And movement videos were recorded by a CCD camera at a frame rate of about 25 frames per second.

### Optimization of assay parameters for MNPs performance

To obtain the best detection performance, the effects of key assay parameters on the operation of MNPs in solution were investigated, including $Fe_3O_4$@$SiO_2$ dosage, conjugation time, reaction temperature, reaction time, magnetic field strength, magnetic field frequency and magnetic field time. In this study, FCM was used to collect the fluorescence signal of a single MNP reacting with miR-21. To collect the fluorescence from individual MNPs, the MNP concentration was maintained at very low level (~50 μg/mL) to minimize proximity-driven aggregation. Several rounds of blowing and mixing were performed to ensure complete dispersion of the particles before loading the sample. The FCM detection was carried out with a 638 nm laser excitation and a total of 10,000 MNPs were collected for each sample. The fluorescence signal triggered by miR-21 could be accurately reflected by ΔF, which means the mean fluorescence intensity (MFI) of MNPs for target detection minus the MFI of the background signal.

### Performance evaluation of MNPs in solution

For evaluating the sensitivity of MNPs, various concentrations of miR-21 were incubated with MNPs (50 μg) in 100 μL TM buffer. Then, the mixed solution was placed into the thermostatic oscilltometer without magnetic field or the magnetic control platform with the external magnetic field. After the reaction, the fluorescence signal was detected using FCM. For evaluating the specificity of MNPs, miR-21 and several different miR-21 analogues were added respectively into TM buffer with a final concentration of 25 nM and incubated with MNPs at 37 °C before FCM analysis.

### Cell culture and cytotoxicity of MNPs

Human embryonic kidney (HEK293), human cervical cancer (Hela), human malignant melanoma (A375) and human breast adenocarcinoma (MCF-7 and MDA-MB-231) cell lines were incubated in DMEM medium supplemented with FBS (10% (v/v) and 1% penicillin/streptomycin). The cells were cultured in a humidified incubator containing 5% $CO_2$ at 37 °C. To assess cytotoxicity of MNPs, the cells were seeded in a 96-well plate with a density of $1 \times 10^4$ cells/well and cultured for 24 h. Then, various concentrations MNPs were added and incubated for 24 h. After the medium was removed, 100 μL of culture medium containing 10% of CCK-8 reagent was added into the above wells and incubated for 1–2 h. Subsequently, the absorbances were determined by microplate reader.

### Performance evaluation of MNPs in living cells

For visualized analysis of fluorescence signal, the interest cells were seeded onto a 20 mm round glass slide in 24-well plate ($3 \times 10^4$ cells/well) for 2 h for attachment. After removing the medium and washing with PBS buffer, 300 μL of MNPs (30 μg/mL) were added and incubated for the required time. Then, the cells were fixed with 4% paraformaldehyde for 10 min, permeabilized with 0.1% Tritonx-100 for 10 min and dyed by 1 μg/mL DAPI solution for 8 min. After washing three times with PBS, the fluorescence of the cells was observed under CLSM (405 nm laser for the excitation of DAPI and 640 nm laser for the excitation of Cy5).

For further quantitative analysis of fluorescence intensity, cells were seeded in 12-well plate ($1 \times 10^5$ cells/well). Then, cells were treated with 500 μL of MNPs for various periods. After the treatments, the cells were digested and washed three times with PBS, and finally resuspended in 500 μL PBS for FCM analysis.

### Quantification of the expression level of miR-21 by qRT-PCR

First, total RNAs from HEK293, Hela, A375, MDA-MB-231 and MCF-7 cells in 6-well plate were extracted by using TRIzol reagent. Then, RNAs were reverse-transcribed according to the instruction from miRNA

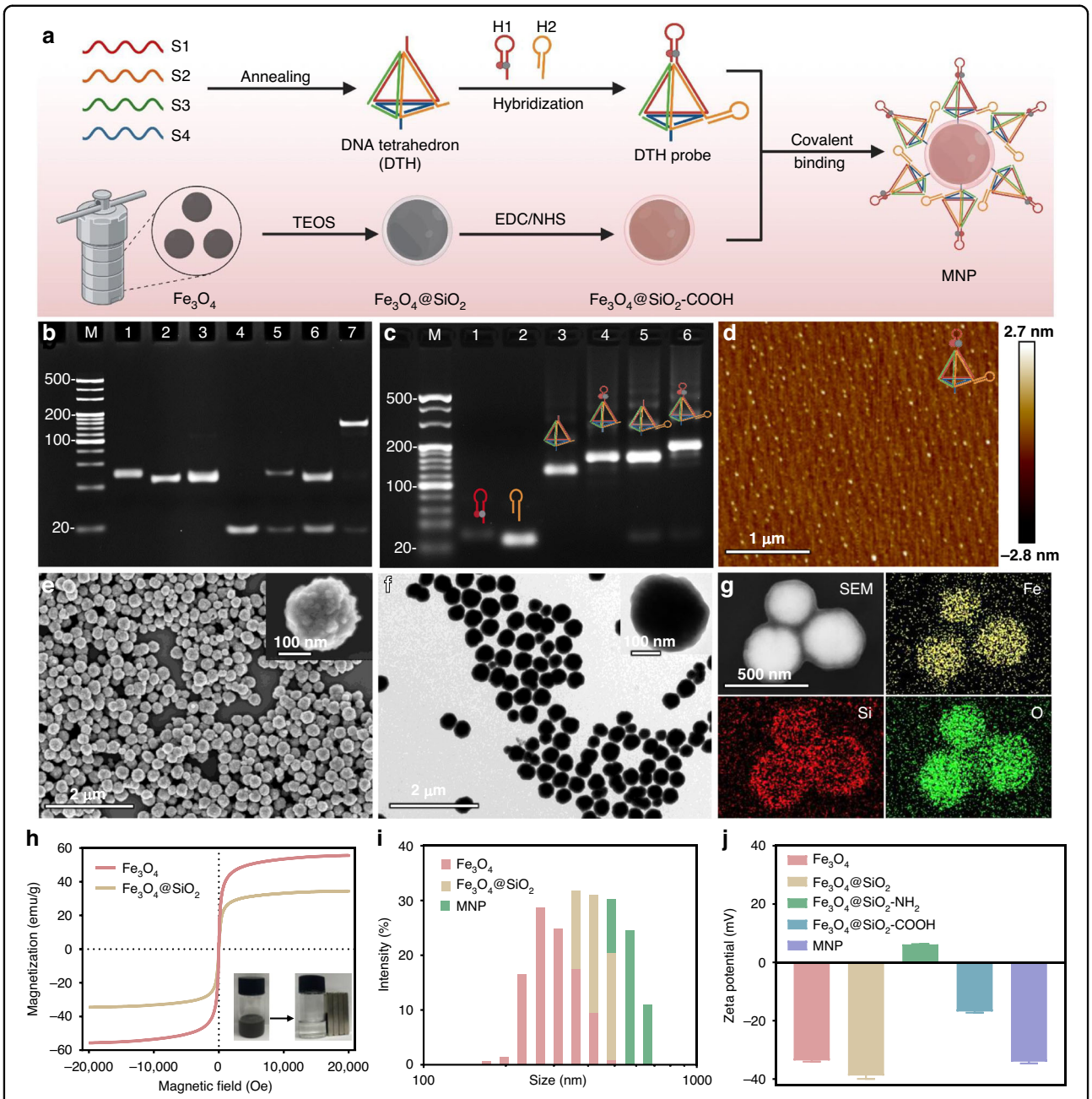


**Fig. 2 Characterization of MNPs. a** Schematic illustration the synthesis process of MNPs. **b** 8% PAGE characterization CHA feasibility (lane M: DNA marker; lane 1, H1; lane 2, H2; lane 3, H1 and H2; lane 4, target; lane 5, H1+target; lane 6, H2+target; lane 7, H1 + H2+target). **c** 3% agarose gel electrophoresis characterization the assembly of DTH probe (lane M, DNA marker; lane 1, H1; lane 2, H2; lane 3, DTH; lane 4, DTH + H1; lane 5, DTH + H2; lane 6, DTH + H1 + H2). **d** AFM image of DTH probe. **e** SEM image of $Fe_3O_4$. **f** TEM image of $Fe_3O_4$@$SiO_2$. **g** EDS element mapping of $Fe_3O_4$@$SiO_2$. **h** Magnetization hysteresis curves of $Fe_3O_4$ and $Fe_3O_4$@$SiO_2$. **i** DLS results of $Fe_3O_4$, $Fe_3O_4$@$SiO_2$ and MNP. **j** Zeta potential of different particles during the synthesis ($Fe_3O_4$, $Fe_3O_4$@$SiO_2$, $Fe_3O_4$@$SiO_2$-$NH_2$, $Fe_3O_4$@$SiO_2$-COOH, MNP). Error bars indicate standard deviation ($n = 3$)

1st Strand cDNA Kit. Finally, the resulting cDNAs were used for fluorescence quantitative PCR using the qPCR Master Mix Kit, and the relative expression level of miR-21 was normalized using the $2^{-\Delta\Delta Ct}$ method with U6 as the internal standard.

## Results and discussion

### Characterization of DTH probes

The assembly strategy of the DTH probe is presented in Fig. 2a. 8% PAGE was first used to verified the feasibility of CHA cycle (Fig. 2b). When the target was incubated

with H1 (lane 5), H2 (lane 6) or H1 + H2 (lane 7), it only specifically unfolded the hairpin structure of H1, with no nonspecific binding with H2. When the target mixed with H1 + H2, it would mediate the formation of the H1-H2 complex to release the target for cycling, and its mobility was the slowest than others (lanes 1–6). These results indicated the successful design of the CHA oligonucleotide sequences with high target recognition ability and low background leakage. Then, 3% agarose gel electrophoresis was used to characterize the self-assembly process of DNA tetrahedral backbone (Fig. S2) and DTH probe (Fig. 2c). With the stepwise addition of ssDNAs, the migration of the DNA assemblers gradually slowed down, and the slowest migration was the DTH probe (Fig. 2c, lane 6), suggesting the successful assembly of the probe. AFM imaging (Fig. 2d) further confirmed the successful formation of DTH probe with monodispersity. Meanwhile, DLS detection (Fig. S3) showed that the hydrodynamic diameter of DTH was ~12 nm and that of DTH probe was ~18 nm. Taken together, these results proved the successful construction of DTH probe and exhibited the feasibility of target detection.

Time-dependent monitoring of the fluorescence signal was used to analyze the reaction kinetics of DTH probes (Fig. S4). DTH probes showed a much faster CHA fluorescence response and a similar background signal compared to free hairpins (Fig. S4a). Specifically, the DTH probe reached the reaction plateau at 2.0 h, while the free hairpin did not show any plateau during the whole reaction process. In addition, the fluorescence signal of all products was detected at the end point of the reaction after 2.5 h. The signal of the DTH probe was 6301, while the free hairpins were 3551, indicating that the spatial confinement effect of DTH enhanced the CHA response signal (Fig. S4b).

To further elucidate the mechanism of the superiority of DTH probes in improving the reaction kinetics and efficiency, several relevant parameters were analyzed by collision theory ($V = 1/cN$), in which $V$ represents sphere volume, $c$ represents probe concentration, and $N$ represents Avogadro constant. In the homogeneous reaction solution, free hairpins were 250 nM and the calculated volume of the sphere was $6.64 \times 10^{-18}$ L, further yielding a sphere radius ($r$) of 117 nm according to the equation $V = 4\pi r^3/3$. For DTH probe, the distance between H1 and H2 was 18.02 nm (53 base pairs including 17 bp for the edge length, 30 bp for tetrahedral frame complementary to the hairpins and 6 bp for spacer). By calculation, the sphere volume of the DTH probe was $2.45 \times 10^{-20}$ L, and based on the spatial confinement effect of DTH, the local concentration of hairpin H1 and H2 was 67.8 μM, which was 271-fold higher than that of the free hairpins (Fig. S5). Therefore, DTH hairpins collided with each other more frequently and the reaction kinetics were proved to be much faster than free hairpins.

### Preparation and characterization of $Fe_3O_4$, $Fe_3O_4$@$SiO_2$ and MNP

The synthetic strategy of MNPs was depicted in Fig. 2a. The $Fe_3O_4$ nanoparticles synthesized by hydrothermal method were monodisperse and uniform sphere with sizes of 240 nm. (Fig. 2e). To prepare carboxyl-rich $Fe_3O_4$, silica was applied to coat $Fe_3O_4$ and then functionalized on its surface. The TEM characterization showed that silica was successfully modified onto the surface of $Fe_3O_4$ with a shell thickness of 20 nm (Fig. 2f and Fig. S6). The core−shell structure was further verified by elemental mapping analysis (Fig. 2g). The Fe element was distributed in the core of $Fe_3O_4$@$SiO_2$, while Si and O appeared throughout the structure. Then, the magnetization curves were used to characterize the magnetic properties of $Fe_3O_4$@$SiO_2$ (Fig. 2h). The saturation magnetization strength (Ms) value of $Fe_3O_4$@$SiO_2$ was 34.45 emu/g, which is smaller than that of uncoated $Fe_3O_4$ (55.60 emu/g). But the high Ms of $Fe_3O_4$@$SiO_2$ and the absence of obvious coercivity and remanence in the curve indicated that the synthesized $Fe_3O_4$@$SiO_2$ had good superparamagnetism. Further, the nanocomposite can be rapidly collected by the external magnetic field, showing excellent magnetic response properties (Fig. 2h). Next, the surface modification process of MNPs were measured by DLS and zeta potential for each step. The average hydrate particle size of $Fe_3O_4$, $Fe_3O_4$@$SiO_2$ and MNP were 267 nm, 361 nm, and 488 nm, respectively (Fig. 2i). Meanwhile, the zeta potential values of $Fe_3O_4$, $Fe_3O_4$@$SiO_2$, $Fe_3O_4$@$SiO_2$-$NH_2$, $Fe_3O_4$@$SiO_2$ $Fe_3O_4$@$SiO_2$-COOH and MNP were -33.62 ± 0.425 mV, -38.82 ± 1.128 mV, 6.168 ± 0.097 mV, -16.81 ± 0.452 mV and -34.03 ± 0.6187 mV, respectively (Fig. 2j). The stepwise change in nanoparticle size and zeta potential during the synthesis process confirmed the successful preparation of MNP.

### Optimization of MNPs detection assay

Given the fast, sensitive, and high-throughput performance of FCM, FCM was used as the signal output platform in this work. The detection procedure was illustrated in Fig. 3a, where MNPs were mixed with samples and placed in a thermostatic oscillator or a 3D Helmholtz coil as a response without or with a magnetic field, respectively. After the reaction, the Cy5 signal intensity of single-particle MNP was measured by using an FCM. We first verified the feasibility of FCM for the detection of fluorescence signals on MNPs. FAM-labeled MNPs showed a clear enhancement of the fluorescence compared with $Fe_3O_4$@$SiO_2$, indicating that conventional flow

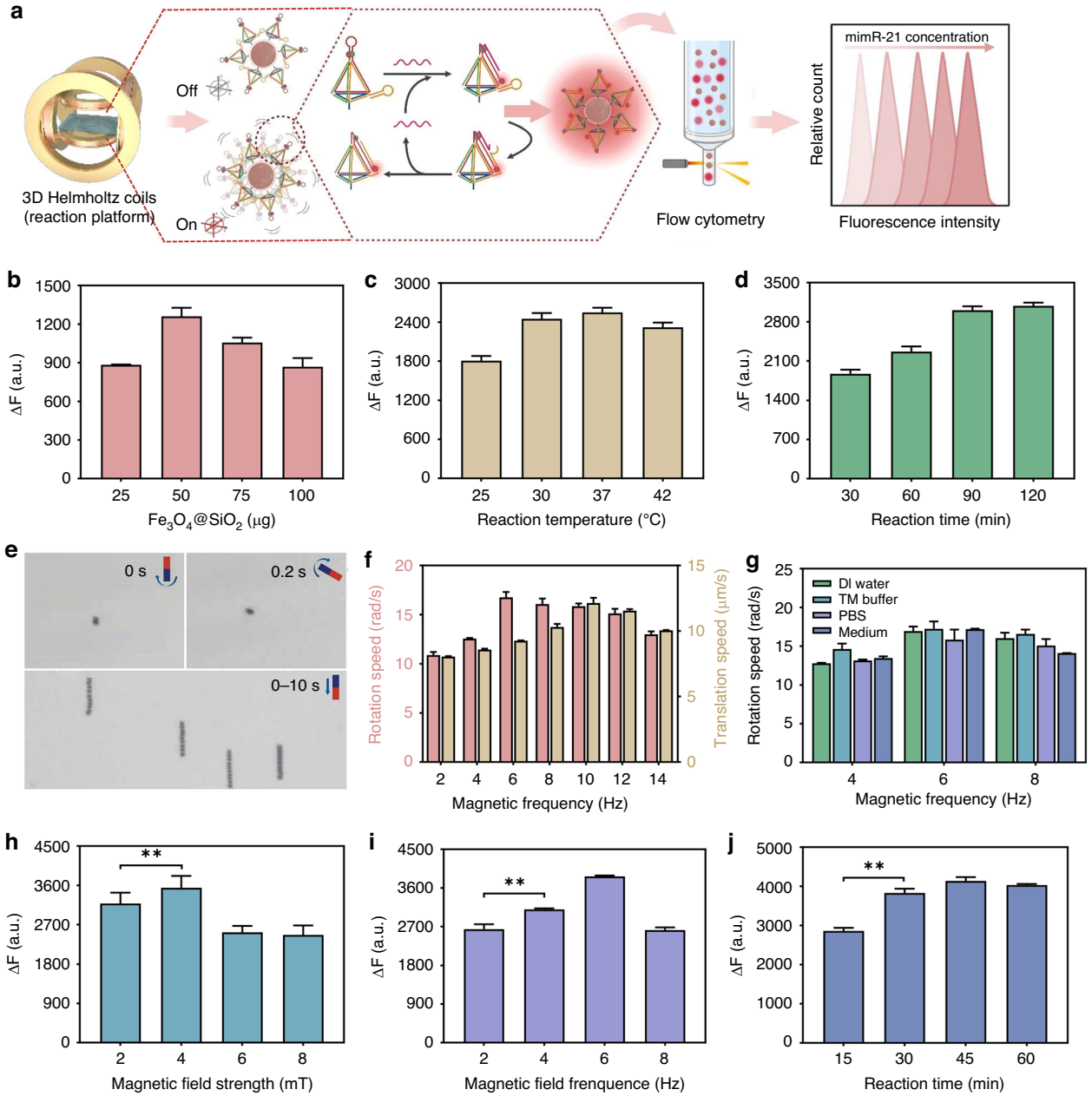


**Fig. 3 Optimization assays of MNPs detecting miR-21 in solution. a** Schematic illustration of MNPs for miR-21 detection with or without rotating magnetic field. Optimization of (**b**) $Fe_3O_4$@$SiO_2$ dosage, (**c**) reaction temperature and (**d**) reaction time without magnetic field. **e** MNP rotation and translation at different time intervals in DI water (frequency of the magnetic field was 6 Hz for rotation and 8 Hz for translation). **f** Rotation and translation speed of MNPs in DI water and (**g**) rotation speed of MNPs in different types of solutions under the rotating magnetic field (4 mT). Optimization of (**h**) magnetic field strength, (**i**) magnetic field frequency and (**j**) reaction time under the rotating magnetic field. Error bars indicate standard deviation ($n = 3$). $^{**}P < 0.01$

cytometry can detect the signal on the surface of MNPs (Fig. S7).

We then optimized the reaction conditions to achieve the best performance of MNPs in response to miR-21 in solution. $Fe_3O_4$@$SiO_2$ dosage, conjugation time of $Fe_3O_4$@$SiO_2$ with DTH probe, reaction temperature and reaction time were determined to be 50 μg, 6 h, 37 °C and 120 min, respectively (Fig. 3b–d, Fig. S8).

In order to explore whether the magnetic field promoted the motion of MNPs, the custom-designed magnetic field generator was used to drive wirelessly the MNPs. When the magnetic field generator produces a

rotating magnetic field parallel to the *XY* plane, the MNPs will self-assemble into rod-like structures and rotate in accordance with the magnetic field under the influence of the torque **T** ($\mathbf{T} = \mathbf{m} \times \mathbf{B}$), where **B** is the external magnetic field and **m** is the magnetic moment. When the plane of the rotating magnetic field is parallel to the *XZ* plane, the MNPs will rotate within the *XZ* plane and produce displacement due to the interaction force between the MNPs and the substrate (Fig. 3e). In the experiment, the rotation and translation speeds of MNPs at different magnetic field frequencies were recorded. As shown in Fig. 3f, both the rotation speed and translation speed initially increased with the rising frequency of the rotating magnetic field, and then began to decrease (Move S1–S2). The frequencies corresponding to the maximum rotation speed and translation speed were 6 Hz and 10 Hz, respectively. Furthermore, we investigated the movement of MNPs in the common solutions: DI water (0.71 cP), TM buffer (~0.82 cP), PBS (~0.83 cP) and cell culture medium (0.93 cP) with different viscosities. The viscosity of the solutions increases slightly from DI water to PBS/TM buffer and further to medium. However, the rotation speeds of MNPs in these different solution environments showed little variation, with the maximum rotation speed remaining at 6 Hz (Fig. 3g). This indicated that the slight differences in viscosity did not significantly affect the rotational dynamics of the MNPs, ensuring their applicability in subsequent experiments.

We further analyzed the effects of the magnetic field-related parameters on the detection performance. MNPs reached the best signal intensity at a rotating magnetic field strength of 4 mT, which was significantly higher than the signal without magnetic field reaction for 30 min (Fig. 3h). We then analyzed the effect of the magnetic field frequency on the response of $Fe_3O_4$@$SiO_2$-DTH probe. The results revealed that the ΔF signal gradually increased with increasing magnetic field frequency and reached the maximum value at 6 Hz (Fig. 3i), so 6 Hz was selected as the optimal magnetic field frequency. Evaluation of the reaction time showed that the ΔF values fluctuated slightly from 30 to 60 min, probably due to the reaction having already reached a plateau during this period (Fig. 3j). We therefore chose 45 min as a further reaction time to ensure that the reaction was fully performed. Finally, we selected 4 mT, 6 Hz and 45 min as the optimal magnetic field parameters for the following experiments.

### Performance of MNPs in solution

The detection performance of MNPs was investigated under the optimal reaction conditions. To evaluate the sensitivity of MNPs' response to target, we recorded the changes in fluorescence intensity (ΔF) after adding various concentrations of the target miR-21 to the reaction. ΔF increased gradually with the target miRNA concentrations increasing from 0 to 500 nM (Fig. 4a–c and Fig. 4d–f). When no magnetic field was applied to the detection system, the linear range of MNPs was 0.5–100 nM, and the limit of detection (LoD) was calculated to be 64.41 pM by the formula 3 s/k (s was the standard deviation of the blank samples and k was the slope of the standard curve) (Fig. 4c), whereas applying a rotating magnetic field, MNPs showed a broader linear range and lower LoD of 0.1–100 nM, and 2.34 pM, respectively (Fig. 2f). Compared to the Brownian motion of MNPs in solution, the magnetic field-driven motion further enhanced the probes' chances of collision with the target, thus improving the detection sensitivity.

Next, to evaluate the specificity of MNPs toward miR-21, given the high similarity in the miRNA sequences, we co-incubated MNPs with various mismatched miR-21 (single-, double-, three- base mismatched sequences, SBM, DBM, and TBM, respectively) and other unrelated targets (miR-155 and miR-221) (Fig. 4j). The ΔF value produced by target miR-21 was significantly much higher than that produced by DBM, TBM and non-target miRNAs (Fig. 4h, i and Fig. 4k, l), revealing that our constructed MNPs had the high specificity for miRNA detection. However, it was noteworthy that MNPs had difficulty distinguishing multiple SBM sequences when no magnetic field was applied. Whereas after the rotating magnetic field was applied, MNPs could effectively recognize SBMs whose mutation sites were located outside of the toehold. Driven by the rotating magnetic field, MNPs would self-assemble into a rod-like structure and their rotating stirring motion can separate the probe from the non-specific and weak binding to the interferents, thus improving the specificity of the assay (Fig. 4g). Overall, the rotating magnetic field significantly enhanced the detection efficiency of MNPs in vitro compared to conditions without a magnetic field, achieving a 2.67-fold reduction in reaction time, a 27.53-fold improvement in the limit of detection (LOD), and more sensitive discrimination of mismatched base sequences. Additionally, we compared our approach with other similar DNA nanoprobes, demonstrating that our strategy is either comparable or superior to several previously reported methods (Table S2).

### Serum stability and cell cytotoxicity of MNPs

To avoid false positive signals and side effects in the cells, the stability and cytotoxicity of MNPs in complex biological environments are important indicators to be evaluated before they are applied to intracellular imaging. The fluorescence spectrum showed that the fluorescence leakage of DTH probes was significantly lower than free H1 in a DMEM medium with 10% FBS (Fig. S9a). Meanwhile, gel electrophoresis analysis also exhibited that the free H1 bands were quickly degraded with the time

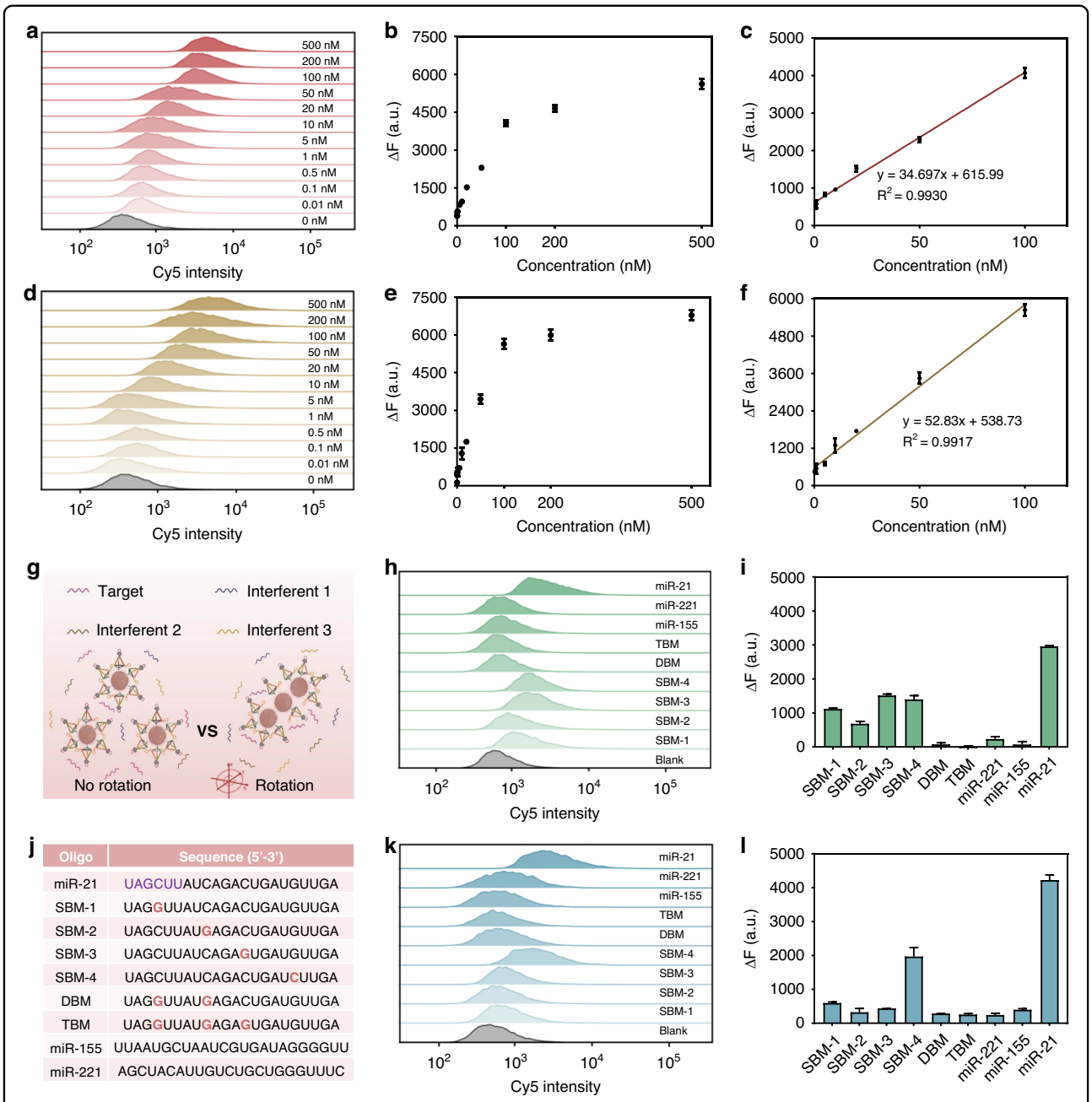


| Oligo | Sequence (5'-3') |
|---|---|
| miR-21 | UAGCUUAUCAGACUGAUGUUGA |
| SBM-1 | UAGGUUAUCAGACUGAUGUUGA |
| SBM-2 | UAGCUUAUGAGACUGAUGUUGA |
| SBM-3 | UAGCUUAUCAGAGUGAUGUUGA |
| SBM-4 | UAGCUUAUCAGACUGAUCUUGA |
| DBM | UAGGUUAUGAGACUGAUGUUGA |
| TBM | UAGGUUAUGAGAGUGAUGUUGA |
| miR-155 | UUAAUGCUAAUCGUGAUAGGGGUU |
| miR-221 | AGCUACAUUGUCUGCUGGGUUUC |

**Fig. 4 Sensitivity and specificity of MNPs.** Flow cytometry histograms for different miR-21 concentrations detection (**a**) without magnetic field and (**d**) with rotating magnetic field. Sensitivity evaluation: ΔF in response to different miR-21 concentrations (**b**, **c**) without magnetic field and (**e**, **f**) with rotating field. **g** Mechanism illustration of rotating magnetic field for enhancing MNPs specificity. **j** Oligonucleotide sequences of miR-21, SBMs, DBM, TBM, miR-221 and miR-155. Red represents the mutation site and purple presents the toehold of miR-21 unfolding H1. Specificity evaluation: ΔF in response to SBM-1, SBM-2, SBM-3, SBM-3, SBM-4, DBM, TBM, miR-155, miR-221 and miR-21 (**h**, **i**) without magnetic field and (**k**, **l**) with rotating field. Error bars indicate standard deviation ($n = 3$)

progressing, while the band of DTH probes remained clearly visible at 6 h, indicating that DTH probes can be stably preserved for a longer time in a simulated physiological environment (Fig. S9b).

When different concentrations of MNPs were incubated with HEK293, MCF-7 and MDA-MB-231 for 24 h, the probe had no obvious cytotoxicity and cell viability above 95% (Fig. S10a). Even at high concentrations (up to 50 μg/mL), cell viability remained above 90% after 48 h (Fig. S10b). Interesting, MNPs can be well taken up by cells which was attributed to the promotion of endocytosis by DNA tetrahedra (Fig. S10c). After endocytosis,

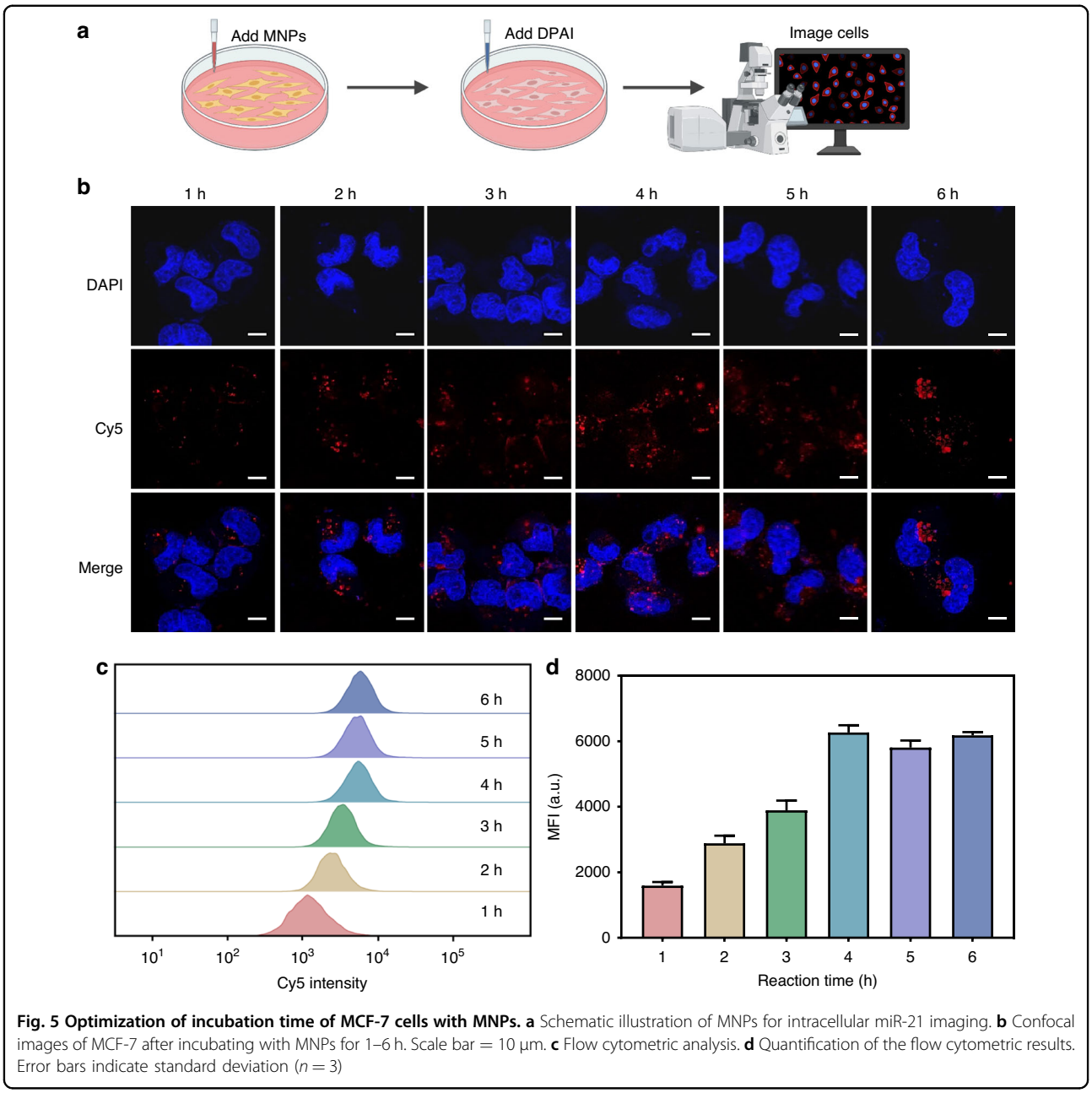


**Fig. 5 Optimization of incubation time of MCF-7 cells with MNPs. a** Schematic illustration of MNPs for intracellular miR-21 imaging. **b** Confocal images of MCF-7 after incubating with MNPs for 1–6 h. Scale bar = 10 μm. **c** Flow cytometric analysis. **d** Quantification of the flow cytometric results. Error bars indicate standard deviation ($n = 3$)

$Fe_3O_4$@$SiO_2$ primarily localize in the cytoplasm and lysosomes without mitochondria or nuclei accumulation[45,46]. In lysosomes, no $Fe_3O_4$@$SiO_2$ was degraded up to 30 days[45]. Some studies also indicated that $SiO_2$-coated $Fe_3O_4$ significantly reduced oxidative stress and prevented alteration of iron homeostasis compared to uncoated $Fe_3O_4$, due to the protective $SiO_2$ layer preventing direct iron core exposure[47]. This distribution and integrality of $Fe_3O_4$@$SiO_2$ minimizes the risk of MNP cytotoxicity and genotoxicity. After incubation for 7 days, $Fe_3O_4$@$SiO_2$ nanoparticles were packed in membrane bound organelles and they were gradually excreted from the cells along the increased incubation time[45]. These results confirmed the long-term stability and biocompatibility of MNPs, making it the ideal probe for intracellular detection and in vivo imaging analysis.

### Performance of MNPs in living cell imaging

After successfully confirming their stability and cellular uptake efficiency, we further investigated the ability of MNPs to recognize and image the target miR-21 in living cells. We first incubated MNPs with MCF-7 cells to exam the optimal response time (Fig. 5a). CLSM results showed that the Cy5 fluorescence signal

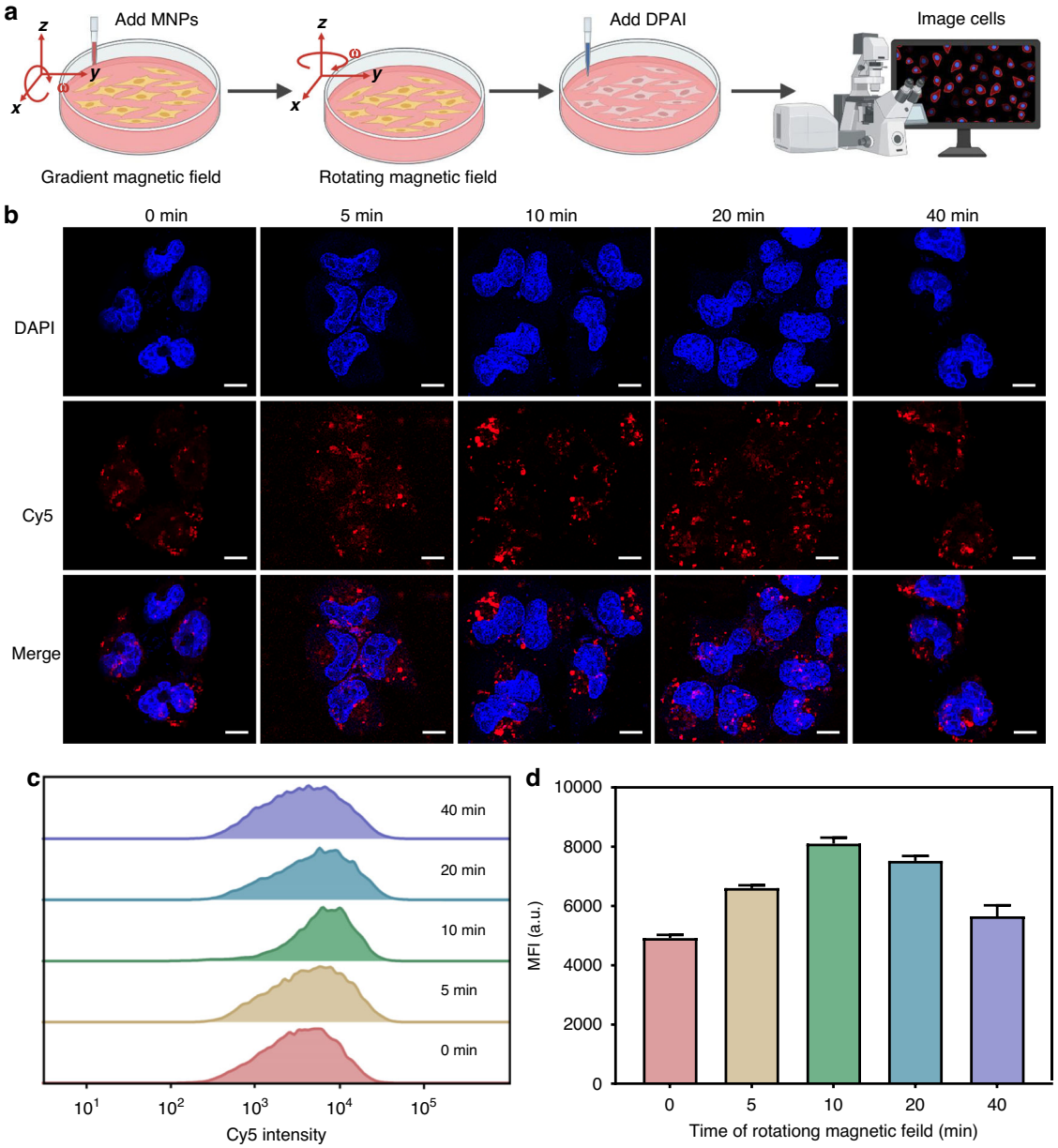


**Fig. 6 Optimization of incubation time of MCF-7 cells with MNPs under the driving of magnetic field. a** Schematic illustration of MNPs for intracellular miR-21 imaging. **b** Confocal images of MCF-7 after incubating with rotating magnetic field (0–40 min). Scale bar = 10 μm. **c** Flow cytometric analysis. **d** Quantification of the flow cytometric results. Error bars indicate standard deviation ($n = 3$)

was gradually increased with the increase of incubation time from 1-4 h and reached a ceiling at 4 h (Fig.5b). There was no significant change in the fluorescence signal when the time was prolonged from 4 h to 6 h. Therefore, 4 h was choose as the appropriate incubation time for intracellular imaging of MNPs. The FCM was consistent with the above results (Fig.5c, d). In parallel, we also incubated MNPs with normal cell HEK293, which showed a very low fluorescence intensity (Fig. S11a, b). These results indicated that MNPs were able to specifically image intracellular miR-21 with low background leakage.

Next, the role of the magnetic field in MNPs intracellular imaging was further explored by monitoring the fluorescence changes at different time points (Fig. 6a). After the cell attachment, a gradient magnetic field was applied underneath the cells for 10 min, which would make MNPs rapidly sink to the cell level. Subsequently, the magnetic field was withdrawn and allowed the MNPs to rapidly enter the cells by endocytosis. After that, a rotating magnetic field was applied for

different time periods. The whole reaction was completed within 2 h. Mechanically, MNPs were driven by the external magnetic field to perform rotational stirring motion, accelerating the recognition of targets in the surrounding high-viscous environment. The CLSM images revealed a significant increase in Cy5 fluorescence as the reaction time of the rotating magnetic field increased to 10 min (Fig. 6b). However, when the reaction time was continuously extended to 40 min, no significant enhancement of fluorescence was observed, indicating that the reaction reached a plateau after only 10 min under the driving of the rotating magnetic field. These results were also confirmed in the flow cytometry analysis (Fig. 6c, d). Overall, the imaging time under magnetic field driven was shortened from 4 to 2 h compared to no magnetic field applied. Otherwise, unlike methods that require transfection reagents, the MNPs used in our work enable direct cellular entry and miRNA recognition[48]. This simplifies the operational workflow and avoids the introduction of additional treatments that could potentially interfere with native miRNA expression.

In view of the excellent effect of the magnetically driven MNPs, the specificity and selectivity of MNPs were further investigated in human normal cell line (HEK293) and different human cancer cell lines (Hela, A375, MDA-MB-231 and MCF-7). Confocal imaging revealed that the fluorescence intensity of Cy5 in HEK293 cells was weak, while in Hela, A375, MDA-MB-231 and MCF-7 cells were sufficiently bright (Fig. 7a). Previous reports agreed that

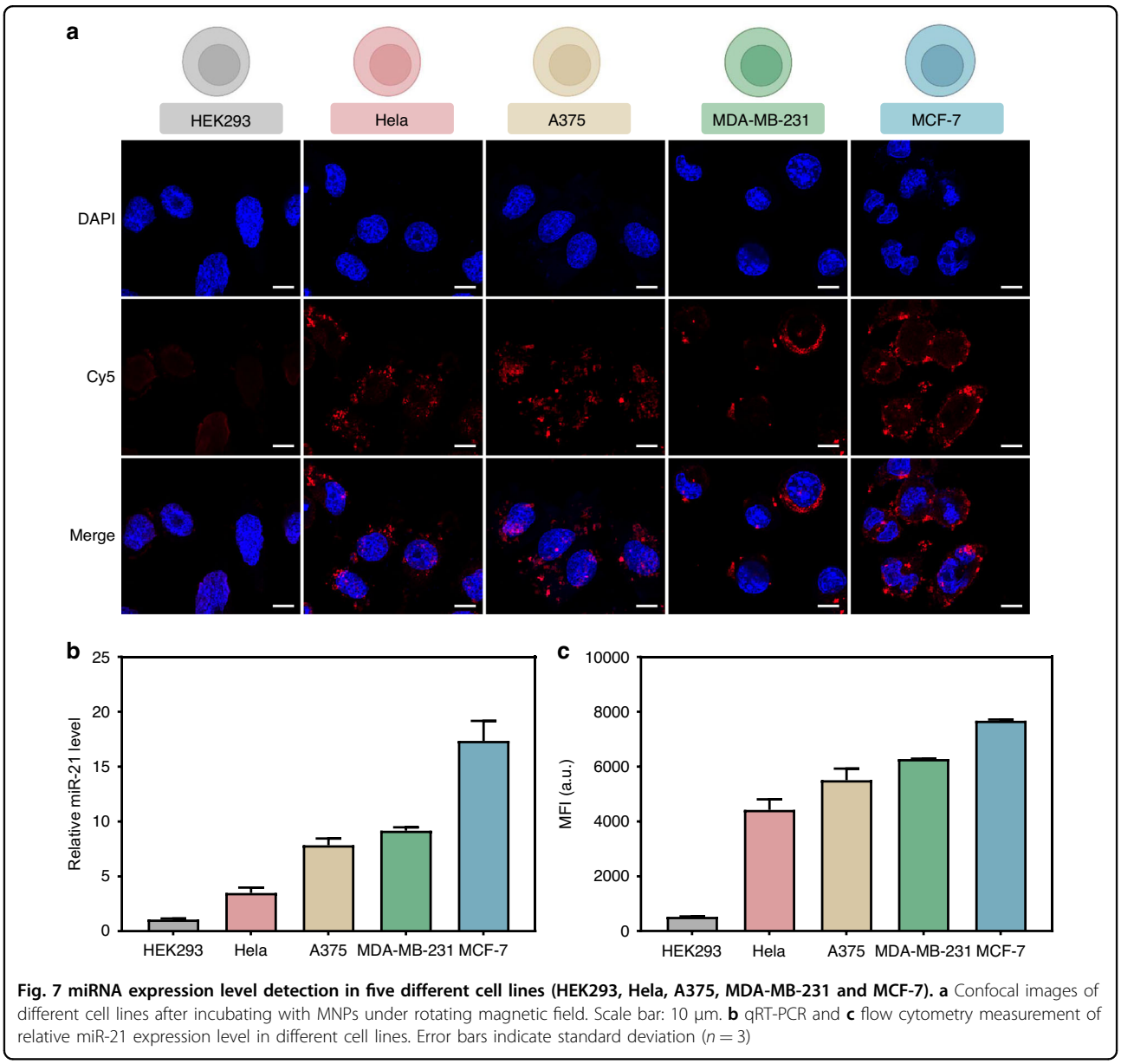


**Fig. 7 miRNA expression level detection in five different cell lines (HEK293, Hela, A375, MDA-MB-231 and MCF-7). a** Confocal images of different cell lines after incubating with MNPs under rotating magnetic field. Scale bar: 10 μm. **b** qRT-PCR and **c** flow cytometry measurement of relative miR-21 expression level in different cell lines. Error bars indicate standard deviation ($n = 3$)

HEK293 expressed lower levels of miR-21 and cancer cells showed higher levels of miR-21[49,50]. Then, we further determined the relative expression levels of miR-21 by qRT-PCR and flow cytometry, all of which were consistent with the confocal images (Fig. 7b, c, Fig. S12). These results suggested that MNPs could effectively identify differential miR-21 expression levels in normal and cancer cells, showing high specificity and versatility.

## Conclusion

In conclusion, we presented the novel DNA tetrahedral-modified magnetic nanorobotic probes (MNPs) for rapid imaging of intracellular cancer-related miRNA. The MNPs were fabricated by combining the magnetically driven nanorobots and the DTH-located CHA probes. In extracellular experiments, magnetic field-driven MNPs significantly shorted the detection time and efficiently identify miR-21, showing higher sensitivity and specificity compared to the magnetic-free driven. In addition, we confirmed that MNPs were low cytotoxic and capable of efficient uptake by the cells. In intracellular experiments, the application of the magnetic field allowed MNPs to rapidly visualize imaging miR-21 and precisely distinguish differences in miR-21 expression levels in different types of living cells. In summary, the magnetically driven MNPs we designed can not only achieve rapidly imaging at specific cancer sites, but also to be used as the flow cytometric probe to detect the differential expression level of cancer-related miRNA, which has great potential for cancer diagnosis and treatment.

#### Acknowledgements

The authors thank the financial support from the National Natural Science Foundation of China (Grants 62122017, 82402730), National Key Research and Development Program of China (Grants 2023YFF0724300, 2023YFF0724304), Natural Science Foundation of Chongqing, China (CSTB2023NSCQ-MSX0728), the Science and Technology Research Program of Chongqing Municipal Education Commission (KJQN202300447). Most schematics were created using BioRender.com.

#### Author details

[1]Key Laboratory of Clinical Laboratory Diagnostics (Ministry of Education), College of Laboratory Medicine, Chongqing Medical University, 400016 Chongqing, China. [2]Department of Academic Research, Beijing Ditan Hospital, Capital Medical University, National Center for Infectious Diseases (Beijing), 100015 Beijing, China. [3]Western Institute of Digital-Intelligent Medicine, 401329 Chongqing, China. [4]Sichuan Provincial Key Laboratory for Human Disease Gene Study, Department of Medical Genetics, Sichuan Academy of Medical Sciences and Sichuan Provincial People's Hospital, University of Electronic Science and Technology, 610072 Chengdu, China. [5]School of Sensing Science and Engineering, Shanghai Jiao Tong University, 200240 Shanghai, China

#### Author contributions

J.H.G. and S.L. contributed to conceive the experiments and revise the manuscript. Y.W. and D.G.L. contributed to formatting changes and final approval of the version to be submitted. X.W. and H.J.B. conducted most of the experiments. L.F.J. contributed to record the motion video of MNPs and analyze the relative data. C.P.M. and Y.L. contributed to perform cell experiments.

#### Competing interests

The authors declare no competing interests.

**Supplementary information** The online version contains supplementary material available at https://doi.org/10.1038/s41378-025-00927-1.

Received: 30 October 2024 Revised: 24 February 2025 Accepted: 19 March 2025
Published online: 27 May 2025

#### References

1. Bray, F. et al. Global cancer statistics 2022: GLOBOCAN estimates of incidence and mortality worldwide for 36 cancers in 185 countries. *Cancer J. Clin.* **74**, 229–263 (2024).
2. Wang, H. et al. Review: RNA-based diagnostic markers discovery and therapeutic targets development in cancer. *Pharmacol. Therapeutics* **234**, 108123 (2022).
3. Yan, H. et al. A one-pot isothermal Cas12-based assay for the sensitive detection of microRNAs. *Nat. Biomed. Eng.* **7**, 1583–1601 (2023).
4. Ferragut Cardoso, A. P., Banerjee, M., Nail, A. N., Lykoudi, A. & States, J. C. miRNA dysregulation is an emerging modulator of genomic instability. *Semin Cancer Biol.* **76**, 120–131 (2021).
5. Krol, J., Loedige, I. & Filipowicz, W. The widespread regulation of microRNA biogenesis, function and decay. *Nat. Rev. Genet.* **11**, 597–610 (2010).
6. Sengupta, D. et al. Dissecting miRNA facilitated physiology and function in human breast cancer for therapeutic intervention. *Semin. Cancer Biol.* **72**, 46–64 (2021).
7. Shang, R., Lee, S., Senavirathne, G. & Lai, E. C. microRNAs in action: biogenesis, function and regulation. *Nat. Rev. Genet.* **24**, 816–833 (2023).
8. Diener, C., Keller, A. & Meese, E. The miRNA–target interactions: an underestimated intricacy. *Nucleic Acids Res.* **52**, 1544–1557 (2023).
9. Kumarswamy, R., Volkmann, I. & Thum, T. Regulation and function of miRNA-21 in health and disease. *RNA Biol.* **8**, 706–713 (2011).
10. Yu, S. et al. Ultrasensitive detection of miRNA-21 by click chemistry and fluorescein-mediated photo-ATRP signal amplification. *Analytica Chim. Acta* **1277**, 341661 (2023).
11. Li, H.-J. et al. Inhibition of miRNA-21 promotes retinal ganglion cell survival and visual function by modulating Müller cell gliosis after optic nerve crush. *Exp. Cell Res.* **375**, 10–19 (2019).
12. Chen, X. et al. Cancer-derived small extracellular vesicles PICKER. *Anal. Chem.* **94**, 13019–13027 (2022).
13. Ždralević, M. et al. Advances in microRNAs as emerging biomarkers for colorectal cancer early detection and diagnosis. *Int J. Mol. Sci.* **25**, 11060 (2024).
14. Zhang, Q. et al. Spatiotemporally programmed disassembly of multifunctional integrated dnazyme nanoplatfrom for amplified intracellular microRNA imaging. *Small* **20**, 2305672 (2024).
15. Xin, M.-K., Sun, X., Tang, H.-W. & Li, C.-Y. Near-infrared light-powered and DNA nanocage-confined catalytic hairpin assembly nanobiosensor with a nucleic acid restriction behavior and reinforced enzymatic resistance for robust imaging assay in live biosystems. *Anal. Chem.* **96**, 7101–7110 (2024).
16. Xue, Y. et al. An ultrasensitive and multiplexed miRNA one-step real time RT-qPCR detection system and its application in esophageal cancer serum. *Biosens. Bioelectron.* **247**, 115927 (2024).
17. Shiino, S. et al. Serum miRNA–based prediction of axillary lymph node metastasis in breast cancer. *Clin. Cancer Res.* **25**, 1817–1827 (2019).
18. Meng, X., Pang, X., Yang, J., Zhang, X. & Dong, H. Recent advances in electrochemiluminescence biosensors for microRNA detection. *Small* **20**, 2307701 (2024).
19. Lin, M. et al. Electrochemical detection of nucleic acids, proteins, small molecules and cells using a DNA-nanostructure-based universal biosensing platform. *Nat. Protoc.* **11**, 1244–1263 (2016).
20. Han, Z. et al. Ultrasensitive detection of mRNA in extracellular vesicles using DNA tetrahedron-based thermophoretic assay. *Nano Today* **38**, 101203 (2021).
21. Zhou, L. et al. Three-dimensional DNA tweezers serve as modular DNA intelligent machines for detection and regulation of intracellular microRNA. *Sci. Adv.* **6**, eabb0695 (2020).

22. Zhang, B. et al. Facilitating in situ tumor imaging with a tetrahedral DNA framework-enhanced hybridization chain reaction probe. *Adv. Funct. Mater.* **32**, 2109728 (2022).
23. Feng, Y. et al. Endogenous mRNA-powered and spatial confinement-derived DNA nanomachines for ultrarapid and sensitive imaging of Let-7a. *Anal. Chem.* **96**, 564–571 (2024).
24. Lin, N. et al. Spatially localized entropy-driven evolution of nucleic acid-based constitutional dynamic networks for intracellular imaging and spatiotemporal programmable gene therapy. *J. Am. Chem. Soc.* **146**, 20685–20699 (2024).
25. Bai, H. et al. Dispersion-to-localization of catalytic hairpin assembly for sensitive sensing and imaging microRNAs in living cells from whole blood. *Biosens. Bioelectron.* **198**, 113821 (2022).
26. Ding, H. et al. DNA nanostructure-programmed like-charge attraction at the cell-membrane interface. *ACS Cent. Sci.* **4**, 1344–1351 (2018).
27. Liang, L. et al. Single-particle tracking and modulation of cell entry pathways of a tetrahedral DNA nanostructure in live cells. *Angew. Chem. Int Ed.* **53**, 7745–7750 (2014).
28. Lin, R., Yu, W., Chen, X. & Gao, H. Self-propelled micro/nanomotors for tumor targeting delivery and therapy. *Adv. Healthc. Mater.* **10**, 2001212 (2021).
29. Liang, Z., Tu, Y. & Peng, F. Polymeric micro/nanomotors and their biomedical applications. *Adv. Healthc. Mater.* **10**, 2100720 (2021).
30. Wang, S. et al. Biocompatibility of artificial micro/nanomotors for use in biomedicine. *Nanoscale* **11**, 14099–14112 (2019).
31. Karaca, G. Y. et al. Gold–nickel nanowires as nanomotors for cancer marker biodetection and chemotherapeutic drug delivery. *ACS Appl. Nano Mater.* **4**, 3377–3388 (2021).
32. Yu, Y. et al. Micro/nanomotor-driven intelligent targeted delivery systems: dynamics sources and frontier applications. *Adv Healthcare Mater.* 2400163 https://doi.org/10.1002/adhm.202400163 (2024).
33. Wang, Q., Yang, S. & Zhang, L. Untethered micro/nanorobots for remote sensing: toward intelligent platform. *Nanomicro Lett.* **16**, 40 (2023).
34. Xu, H., Medina-Sánchez, M., Maitz, M. F., Werner, C. & Schmidt, O. G. Sperm micromotors for cargo delivery through flowing blood. *ACS Nano* **14**, 2982–2993 (2020).
35. Chen, Y. et al. Carbon helical nanorobots capable of cell membrane penetration for single cell targeted SERS bio-sensing and photothermal cancer therapy. *Adv. Funct. Mater.* **32**, 2200600 (2022).
36. Jiang, L. et al. Intelligent sensing based on active micro/nanomotors. *J. Mater. Chem. B* **11**, 8897–8915 (2023).
37. Cao, Q. et al. MOF-based magnetic microrobot swarms for pH-responsive targeted drug delivery. *Sci. China Chem.* https://doi.org/10.1007/s11426-023-1875-7 (2024).
38. Zhang, X., Chen, C., Wu, J. & Ju, H. Bubble-propelled jellyfish-like micromotors for DNA sensing. *ACS Appl. Mater. Interfaces* **11**, 13581–13588 (2019).
39. Fu, S., Zhang, X., Xie, Y., Wu, J. & Ju, H. An efficient enzyme-powered micromotor device fabricated by cyclic alternate hybridization assembly for DNA detection. *Nanoscale* **9**, 9026–9033 (2017).
40. Wu, J. et al. Enzymatic/magnetic hybrid micromotors for synergistic anticancer therapy. *ACS Appl. Mater. Interfaces* **13**, 31514–31526 (2021).
41. Esteban-Fernández De Ávila, B. et al. miRNA single cell real-time miRNAs sensing based on nanomotors. *ACS Nano* **9**, 6756–6764 (2015).
42. Wang, Y. et al. Magnetic nanorobots as maneuverable immunoassay probes for automated and efficient enzyme linked immunosorbent assay. *ACS Nano* **16**, 180–191 (2022).
43. Liu, J. et al. Highly water-dispersible biocompatible magnetite particles with low cytotoxicity stabilized by citrate groups. *Angew. Chem. Int. Ed.* **48**, 5875–5879 (2009).
44. Wang, Y. et al. Magnetic nanomotor-based maneuverable SERS probe. *Research (Wash., D. C.)* **2020**, 7962024 (2020).
45. Tian, F. et al. Fates of $Fe_3O_4$ and $Fe_3O_4$@$SiO_2$ nanoparticles in human mesenchymal stem cells assessed by synchrotron radiation-based techniques. *Biomaterials* **35**, 6412–6421 (2014).
46. Kim, J. S. et al. Toxicity and tissue distribution of magnetic nanoparticles in mice. *Toxicological Sci.* **89**, 338–347 (2006).
47. Malvindi, M. A. et al. Toxicity assessment of silica coated iron oxide nanoparticles and biocompatibility improvement by surface engineering. *PLoS ONE* **9**, e85835 (2014).
48. Xie, C. et al. Efficient intracellular microRNA imaging based on the localized and self-sustainable catalytic DNA assembly circuit. *Anal. Chem.* **95**, 10398–10404 (2023).
49. Liu, L. et al. Efficient and reliable microRNA imaging in living cells via a fret-based localized hairpin-DNA cascade amplifier. *Anal. Chem.* **91**, 3675–3680 (2019).
50. Zhang, M. et al. Zipper-confined DNA nanoframe for high-efficient and high-contrast imaging of heterogeneous tumor cell. *Anal. Chem.* **96**, 2253–2263 (2024).